Phase speciation and surface analysis of copper phosphate on high surface area silica support by in situ XAS/XRD and DFT: Assessment for guaiacol hydrodeoxygenation

E. Puzenat, Wanwitoo Wanmolee, Narongrit Sosa, Anchalee Junkaew, Saran Youngjan, Christophe Geantet, Pavel Afanasiev, Dorothée Laurenti, Kajornsak Faungnawakij, Pongtanawat Khemthong

Version of Record: https://www.sciencedirect.com/science/article/pii/S0169433221026258
Manuscript_fbaa9e4526ce193eae13ffd5e29d8534

Phase speciation and surface analysis of copper phosphate on high surface area silica support by *in situ* XAS/XRD and DFT: Assessment for guaiacol hydrodeoxygenation

Wanwitoo Wanmolee [a†], Narongrit Sosa [a†], Anchalee Junkaew [a†], Saran Youngjan [a], Christophe Geantet [b,*], Pavel Afanasiev [b], Eric Puzenat [b], Dorothée Laurenti [b], Kajornsak Faungnawakij [a], and Pongtanawat Khemthong [a,*]

[a] *National Nanotechnology Center (NANOTEC), National Science and Technology Development Agency (NSTDA), Pathum Thani 12120, Thailand*

[b] *Institut de Recherches sur la Catalyse et l'Environnement de Lyon (IRCELYON), UMR 5256, CNRS-Université Claude Bernard Lyon 1, 2 Ave. Albert Einstein, 69626 Villeurbanne, cedex, France*

[†]These authors contributed equally to this work.

*Corresponding author 1: E-mail address: pongtanawat@nanotec.or.th

*Corresponding author 2. E-mail address: christophe.geantet@ircelyon.univ-lyon1.fr

Abstract

In situ characterization has become indispensable technique in the heterogeneous catalyst development because it provides insights into the composition and fundamental nature of materials in a dynamic process. In this work, *in situ* analysis including X-ray absorption spectroscopy (XAS) and X-ray diffraction (XRD) could disclose phase transition via several intermediates during the reduction of copper phosphate precursor ($CuHPO_4.H_2O$) to copper phosphide on high surface silica support (Cu_3P/SiO_2). The synthesized Cu_3P/SiO_2 was further used as a catalyst for hydrodeoxygenation (HDO) reaction of guaiacol, a well-known representative model compound in lignin-derivatives upgrading. Many major products, such as cyclic hydrocarbons, demethylated, deoxygenated, and methylated compounds, were detected in the reaction mixture. The highest selectivity of catechol (72 mol%) was obtained at reaction condition of 300 ºC and 50 bar H_2 after 150 min. The density-functional theory (DFT) calculations revealed the local electronic charge nature and the different roles of Cu and P active sites towards the interaction between reactants/intermediates and the Cu_3P surfaces. The findings of the phase transition during the Cu_3P synthesis and its catalytic activity to the guaiacol HDO reaction, the first to be reported, is beneficial for improving the efficiency metal phosphide-based catalyst for lignin-derived bio-oil into biofuels in the future.

Keywords: *In situ* XAS/XRD; Copper phosphide; Density-functional theory; Guaiacol; Hydrodeoxygenation

1. Introduction

In heterogeneous catalysis, understanding the distinct structural, chemical, and compositional nature of active sites is decisive for developing an efficient catalyst for a chemical reaction. For decades, many novel methods including experimental and computational methods have been continuously developed and applied in this field.[1, 2] For experimental investigation, *in situ* characterization techniques such as *in situ* transmission electron microscopy (TEM), *in situ* Raman spectroscopy, *in situ* UV-Raman spectroscopy, *in situ* X-ray absorption spectroscopy (XAS), *in situ* X-ray diffraction (XRD) and so on have been well developed and greatly provided the information of dynamics toward a coordination environment or the process–structure–property relationship of materials.[1, 3, 4] *In situ* XAS and XRD analyses are especially critical in providing information about microstructure, chemical composition, speciation of active sites as well as dynamic phenomena in many heterogeneous catalytic reactions.[5-8] For computational investigation, a density-functional theory (DFT) is one of the most powerful methods for probing structure, electronic charge details and phenomena in atomic scale.[1, 2] This method can disclose many fundamental aspects (*i.e.* the interaction of intermediates and active sites, reaction mechanism, thermodynamics, etc.), which are still challenging to be obtained from experimental techniques. Nowadays, integrated *in situ* characterizations and computational studies can be used to accelerate discovery and to develop novel heterogeneous catalysts.[9-11]

Typically, deoxygenation (DO) process is well established. It has gained more attention for upgrading the oxygenated compounds derived from lignocellulosic biomass to various biochemicals and valuable biofuels.[12-14] The main DO reaction consists of hydrodeoxygenation (HDO), decarbonylation (DCO), and decarboxylation (DCO_2).[15] HDO is the pathway to remove oxygen atoms from oxygenated compounds in a form of water (H_2O) to

produce hydrocarbons with the same number of carbon atoms.[11, 15] It is preferable than the DCO and DCO_2 routes, which release carbon monoxide (CO) and carbon dioxide (CO_2), in terms of retaining carbon atoms, environmental safety, and economic prospect. In literature, various catalysts such as noble metals (*i.e.* Pt, Pd, Ru, and Rh),[16-19] non-noble metals (*i.e.* Ni, Mo, Co, Fe),[20-25] and metal supported catalysts[26-30] have been employed in the HDO reaction for upgrading the lignin-derived bio-oil.

Several kinds of transition metal phosphides such as FeP, Ni_2P, Ni_3P, $Ni_{12}P_5$, CoP, MoP, FeMoP, NiMoP, WP, and Cu_3P[11, 15, 23, 31-34] have emerged as a promising group of high activity, high stability, and excellent catalytic performance to remove oxygen content for the upgrading of oxygenated compounds. Among these transition metal phosphides, Ni_2P has been widely investigated. However, Ruangudomsakul and co-workers [35] reported that pure phases of Ni_2P is difficult to be synthesized. Moreover, Ni_2P phase is not stable, and it changes during the HDO reaction to another $Ni_{12}P_5$ phase under the presence of hydrogen. Recently, copper phosphide (Cu_3P) has been suggested to be an interesting catalyst for studying the HDO reaction because Cu_3P phase is easier to be obtained and remarkably stable throughout the reaction. Only a few studies reported about HDO of bio-oil model compounds using copper phosphide on silica support (Cu_3P/SiO_2).[35, 36] Until now, there has been no insight into the role of structural properties of copper phosphide catalyst and its catalytic behavior for HDO of lignin model compound.

Therefore, in the present study, a combination of *in situ* XAS/XRD and DFT methods was utilized to gain deep insight into (i) the Cu_3P/SiO_2 synthesis process, (ii) the nature of active sites (iii) its potential catalytic activity towards lignin-derivatives upgrading via the guaiacol HDO reaction. Guaiacol, the most abundant lignin-derived bio-oil compounds, is typically used

as a model compound for the study of kinetics, reaction pathway, and stability of catalysts in the HDO reaction.[37, 38] To the best of our knowledge, no experimental evidence for this proposed study has been reported.

2. Experimental section

2.1 Chemicals and materials

Commercial SiO_2 with BET surface area of 500 $m^2 \cdot g^{-1}$ was supplied from Grace Davison, UK. Guaiacol (99%) and dodecane (99%) were purchased from Acros Organics, France. Catechol (99%), anisole (99%), cresol (99%), phenol (99%), 1,3-dimethylcyclohexane (98%), benzene (99.8%), hexadecane (99%), cyclohexane (99%), cyclohexene (99%), methylcyclohexane (99%), xylenol (99%), copper(II) nitrate hemi(pentahydrate) ($Cu(NO_3)_2.2.5H_2O$), 99%), and ammonium phosphate dibasic ($(NH_4)_2HPO_4$, 99%) were purchased from Sigma-Aldrich, USA. High purity hydrogen (grade B, 99.99%) was used in the experiments. All chemicals were used as received.

2.2 Synthesis of silica-supported copper phosphide

The precursor $CuHPO_4.H_2O$ was synthesized by wet impregnation with the required mole ratio of Cu to PO_4 equivalent to 1:2, according to our previously reported procedure. [38, 39] Briefly, the aqueous solutions of 3.0 mmol $Cu(NO_3)_2 \cdot 2.5H_2O$ salt-containing Cu and $(NH_4)_2HPO_4$ were added dropwise onto SiO_2 (Grace Davison, specific BET area ~500 m^2/g) and continuous stirred for 30 min, followed by ultrasonication using GT-SONIC (GT model:GT-2013QTS, Ultrasonic power 300 W, Frequency 33/40 kHz) at 60 ºC for 3 h to extend the dispersion of Cu metal particles onto the catalyst surface. The obtained phosphate precursor

mixture was dried at room temperature overnight. After impregnation, the catalyst was loaded into a quartz U-tube reactor and calcined in airflow (45 mL·min^{-1}) at 450 ºC for 3 h at a heating rate of 5 ºC min^{-1} to form metal phosphate, namely $Cu_2P_2O_7$. Further, this catalyst $Cu_2P_2O_7$ was reduced under the H_2 flow (50 mL·min^{-1}) at 550 ºC for 5 h at a heating rate of 5 ºC·min^{-1} to obtain Cu_3P before performing the guaiacol HDO tests.

2.3 Catalyst characterization

X-ray diffraction (XRD) was performed by PANalytical X'Pert MPD Pro using Cu-Kα (0.15406 nm) radiation generated at 25 mA current and 50 kV voltage. The XRD patterns were collected in the 2θ range from 5º to 85º with a scan step of 0.33º and a scan rate of 0.1s·step^{-1}. The most intense diffraction peak without overlapping with others was chosen to determine crystalline sizes. *In situ* XRD profiles were recorded at every 50 ºC in the 2θ range of 6º to 66º with a scan step of 0.33º and a scan rate of 0.1 s·step^{-1}. Morphology of the reduced sample was analyzed by transmission electron microscope (TEM) on JEOL2100 Plus at an operating voltage of 200 kV. The temperature-programmed reduction (TPR) was operated from ambient temperature up to 650 ºC under H_2 flow of 20 mL·min^{-1} with a heating rate of 2 ºC·min^{-1}.

2.4 Ex situ X-ray absorption (XAS)

The experiments were carried out at Beamline BM30 of FAME, the French Absorption Spectroscopy Beamline in Material and Environmental Sciences, European Synchrotron Radiation Facility (ESRF), Grenoble, France. Prior to the measurement, a reduced sample, and cellulose powder were mixed, pelletized, and placed onto a sample holder. The Cu K-edge

spectra from X-ray absorption near-edge spectroscopy (XANES) were calibrated by a Cu metal foil and collected in a transmission mode using a Si(111) monochromator.

2.5 In situ XAS experiments

Both XANES and extended X-ray absorption fine structure (EXAFS), were done at the SUT-NANOTEC-SLRI XAS Beamline 5.2, Synchrotron Light Research Institute (Public Organization), Nakhon Ratchasima, Thailand. The calcined sample was pelletized into a diameter of 1.5 cm and placed onto a sample holder.[39, 40] The Cu K-edge spectra were collected in a transmission mode using a Ge(220) as a monochromator. *In situ* XAS experiment was carried out in a high-temperature chamber under a H_2 flow of 20 $mL \cdot min^{-1}$ from ambient temperature up to 550 ºC with a heating rate of 1 $ºC \cdot min^{-1}$. Data reduction and curve fitting were performed by the ATHENA package in the DEMETER version 0.9.25.[41] The k^2 weighted EXAFS function $\chi(k)$ data was Fourier-transformed with a k range between 2.7 to 14.1 $Å^{-1}$ and an R range between 1 to 3 Å. The quality of curve fitting was evaluated using the EXAFS reliability factors (less than 0.04), which indicated misfit related to the experimental data.

2.6 HDO experiments for screening catalytic test

The catalytic activity of Cu_3P/SiO_2 catalyst was preliminary evaluated in HDO reaction of guaiacol. The screening test was carried out in a batch reactor as described in Supplementary Information (SI).

2.7 DFT method and models

A plane wave-based density functional theory implemented in VASP[42, 43] was used to gain more understanding about the active sites on the catalyst surface. The projector-augmented wave (PAW)[44] with the generalized gradient approximation (GGA) refined by Perdew, Burke, and Ernzerhof (PBE)[45] were applied. The energy cutoff of 400 eV was set. We included the dispersion effect by using Grimme's DFT-D3 method.[46] Gaussian smearing method with a sigma of 0.05 was used. The criteria for the optimization were 1×10^{-6} eV and 0.025 eV·Å^{-1} for energy convergence and force convergence, respectively. The spin-unrestricted calculation was applied in all cases. The (100) and (113) surfaces were selected because they were the predominant peaks from XRD measurement (see **Fig. 1(a)**). More details are described in SI. Those surfaces were cleaved from the optimized bulk Cu_3P crystal (see **Fig. S4(b)** in SI). The adsorption energies (E_{ad}) of guaiacol and H_2 were calculated by the following equation.

$$E_{ad} = E_{surf\text{-}X} - E_{surf} - E_X$$

The $E_{surf\text{-}X}$ denotes the total energy of molecule X on a surface while the E_{surf} and E_X terms represent the total energies of the bare surface and the isolated molecule X.

3. Results and discussion

3.1 Structural characteristics by ex situ XRD

Ex situ XRD pattern of a silica-supported copper sample after reduction is depicted in **Fig. 1(a)**. A broad peak from 10 to 35º is attributed to the characteristic of amorphous silica.[47] The XRD pattern is similar to the characteristics of Cu_3P (JCPDS 01-071-2261) with a $P6_3cm$ space group. The six most intense peaks at 36.0, 39.1, 41.6, 45.1, 46.2, and 47.3º are attributed to

the diffraction planes, so-called crystal facets or surfaces of (112), (202), (211), (300), (113) and (212), respectively. Remarkably, two planes at (300), as a parallel crystal plane of (100), and (113) are predominant in the space group. Yuan et al. [48] reported that the second most intense XRD peak of the (312) facet from $Ni_{12}P_5$ catalyst improved the hydrodechlorination of trichloroethylene. Hence, these crystal facets of (100) and (113) were selected for further theoretical study by DFT due to the high possibility of exposure to several entering molecules during reaction testing. The morphology of the reduced sample by TEM is shown in **Fig. 1(b)**. The spherical particles of Cu_3P after the reduction with an average size of about 5.6 nm (see the histogram in the inset) are well dispersed throughout the silica surface. Comparing to our previous study,[49] Cu_3P nanoparticles on silica had a smaller size-range than that on ultra-stable zeolite Y (USY), possibly due to the strong interaction between the nanoparticles and the support surface.

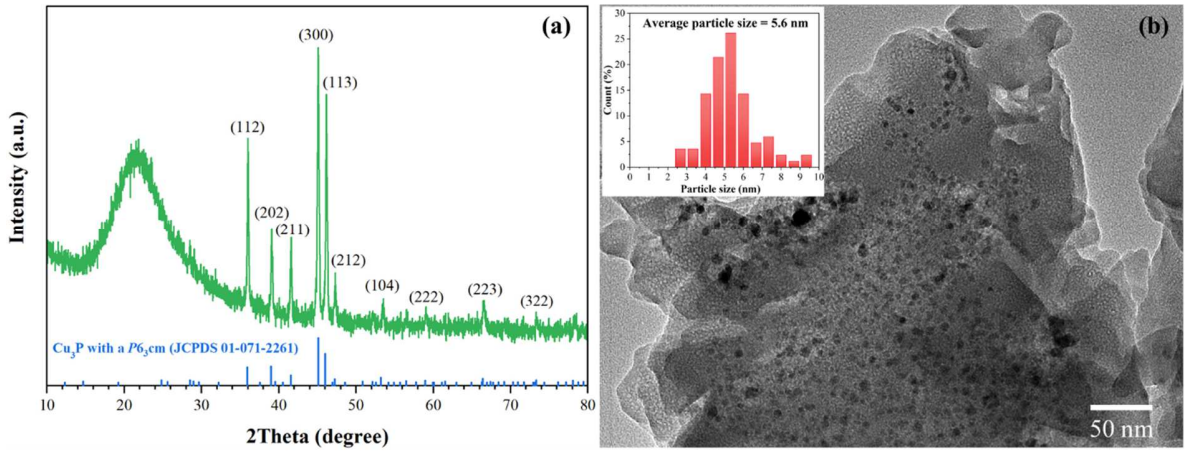

Fig. 1. XRD pattern (a) and TEM image (b) of the reduced silica-supported copper sample with a histogram showing particle size distribution (inset).

3.2 Phase transformation of silica-supported copper species by in situ XRD

The chronological phase transformation of the copper intermediates is crucial to unravel. The H_2 temperature-programmed reduction was followed *in situ* by collecting XRD patterns from room temperature up to 650 ºC as shown in **Fig. 2** and **Fig. S1** (see Supplementary information for comparison to standard XRD patterns). The characteristic phase of $CuHPO_4.H_2O$ precursor (JCPDS 04-016-4434) is still observed up to 250 ºC while XRD intensities decrease with a higher reduction temperature than 50 ºC as a result of successive dehydration of water from its structure. At 250 ºC, diffraction peaks of $Cu_2P_2O_7$ (JCPDS 04-013-9704) are predominant with copper metal (Cu^0) (JCPDS 01-071-4610). During the formation of Cu^0, the $Cu_2P_2O_7$ intermediate could partially decompose towards relevant phosphorus species, not detectable by XRD, namely phosphorus pentoxide (P_2O_5)[50] and phosphines (PH_3) [7, 49] as proposed in the chemical reaction (1-2). Under the reducing atmosphere, Stinner et al. [50] explained that better diffusion of formed water led to the higher transformation of P_2O_5 to the elemental P (P_2 or P_4 in equilibrium) as presented in the reaction (3). Moreover, they also reported that phosphine might also decompose to the elemental P and H_2 in the presence of zerovalent metals as proposed in the reaction (4). Notably, the elemental P does not sublimate at a temperature lower than 416 ºC but is not detected by XRD because of its weak diffraction coefficient.[51]

$$Cu_2P_2O_7 + 2H_2 \longrightarrow 2Cu + P_2O_5 + 2H_2O \quad (1)$$

$$Cu_2P_2O_7 + 10H_2 \longrightarrow 2Cu + 2PH_3 + 7H_2O \quad (2)$$

$$P_2O_5 + 5H_2 \longrightarrow P_2 + 5H_2O \quad (3)$$

$$2PH_3 \longrightarrow P_2 + 3H_2 \quad (4)$$

At 300 ºC, the $Cu_2P_2O_7$ intermediate is transformed into copper pyrophosphate ($Cu(PO_3)_2$, JCPDS 04-016-4419) while the phase of Cu^0 still exists. The first appearance of Cu_3P

(JCPDS 04-004-8619) with a hexagonal *P*-3c1 space group is detectable at 400 ºC with gradual decreases of the mixed phases of $Cu(PO_3)_2$ and Cu^0. The formation of Cu_3P might be similar to the case of CoP formed in CoNiBP alloy during PH_3 decomposition reported by Li et al.[52] We proposed that the elemental P from the decomposition of phosphorus compounds (see reaction (3)-(4)) at a temperature close to its sublimation point could migrate onto the metallic copper particles to form the Cu_3P phase. Up to 450 ºC, both of the latest intermediates were completely converted into the single Cu_3P phase (JCPDS 04-007-2131) with a hexagonal *P*-3m1 space group. Moreover, the crystallite sizes of Cu_3P were progressively developed until 650 ºC, confirmed by increasing peak intensities. After cooling down, the space group of Cu_3P changed to $P6_3cm$ (JCPDS 01-071-2261) due to the rearrangement of the crystal structures. Remarkably, two crystal facets at (300), equivalent to (100), and (113) at around 45.1º and 46.2º, respectively, are still predominant in all space groups of such Cu_3P phases.

3.3 Local atomic structure and chemical bonding by XAS

XAS techniques including XANES and EXAFS were performed to clarify the electronic structure and atomic coordination. XANES spectra and absorbance derivatives at Cu K-edge of the reduced samples and copper references consisting of Cu foil, Cu_2O, and CuO are shown in **Fig. 3**. From the Cu K-edge spectra in **Fig. 3(a)**, the spectrum features of the reduced sample are different from the references but are similar to those of copper phosphide reported in the literature.[53] This implies that the copper precursor on the silica support transforms into copper phosphide after H_2 reduction at 550 ºC, which is in good agreement with the XRD results. As shown in **Fig. 3(b)**, the pre-edge feature of the reduced sample was well fitted with the Cu_2O reference indicating that the oxidation state of atomic copper is monovalence.

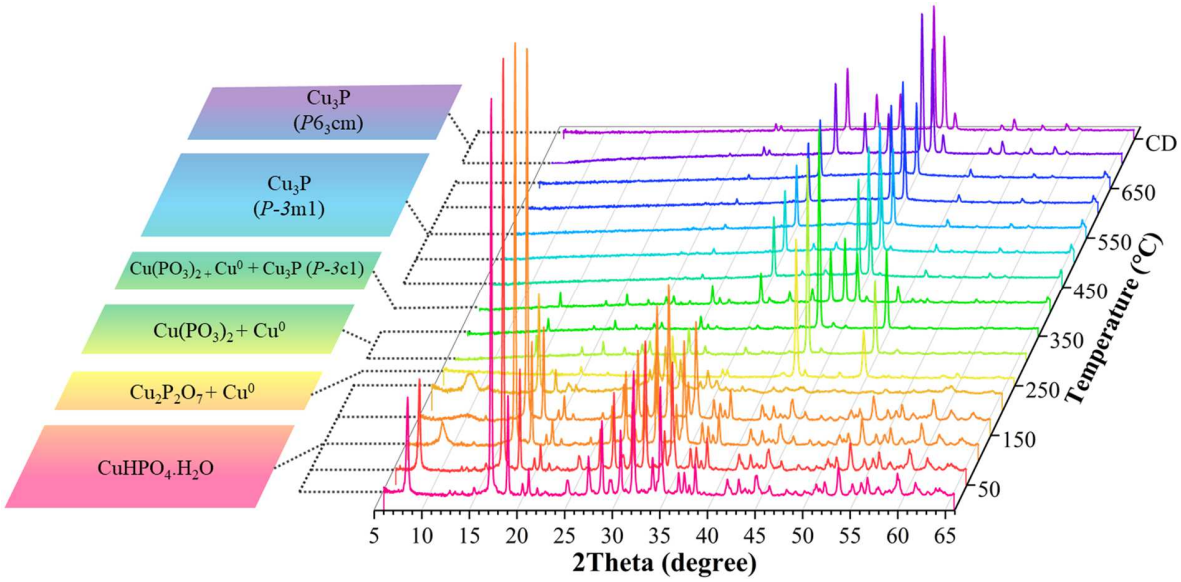

Fig. 2. *In situ* XRD patterns monitoring performed during the H_2-TPR of the $CuHPO_4.H_2O$ precursor of silica-supported copper phosphide (CD = cool down).

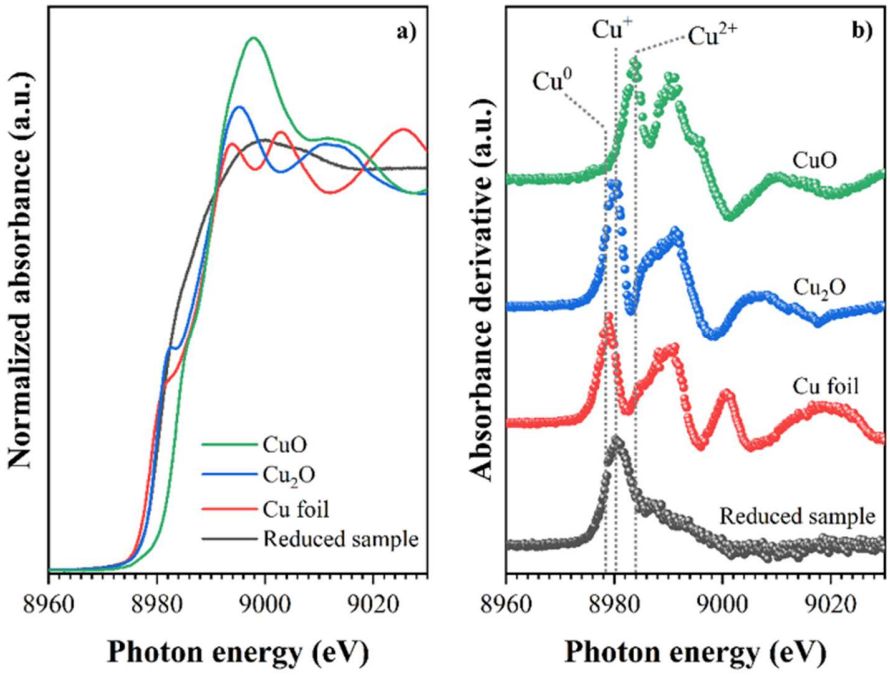

Fig. 3. XANES spectra (a) and 1st derivative at Cu K-edge (b) of the reduced sample compared with Cu foil, Cu_2O, and CuO references.

The change of local atomic structures of the calcined sample monitored during H_2-TPR steps was also monitored by *in situ* XAS to provide complementary evidence. Both *in situ* XANES spectra and the first absorbance derivatives at Cu K-edge are illustrated in **Fig. 4**. **Fig. 4(a)** shows that below 110 ºC, the Cu^{2+} species in the $CuHPO_4.H_2O$ precursor has bivalent characters at the edge energy of 8982 eV together with the white line at 8986 eV corresponding to 1s → 4p transition. At 130 ºC, the edge peak suddenly shifts to lower energy which belongs to the copper monovalence (Cu^+), whereas the spectrum feature of the parent phase is still observed. Meanwhile, the white line intensities dramatically decrease with the increment of reduction temperature until 200 ºC as a result of the consecutive elimination of water.[54] Moreover, the change of neighboring atomic environments of the local Cu sites is also notified by Fourier transformed (FT) EXAFS spectra as shown in **Fig. 5**.

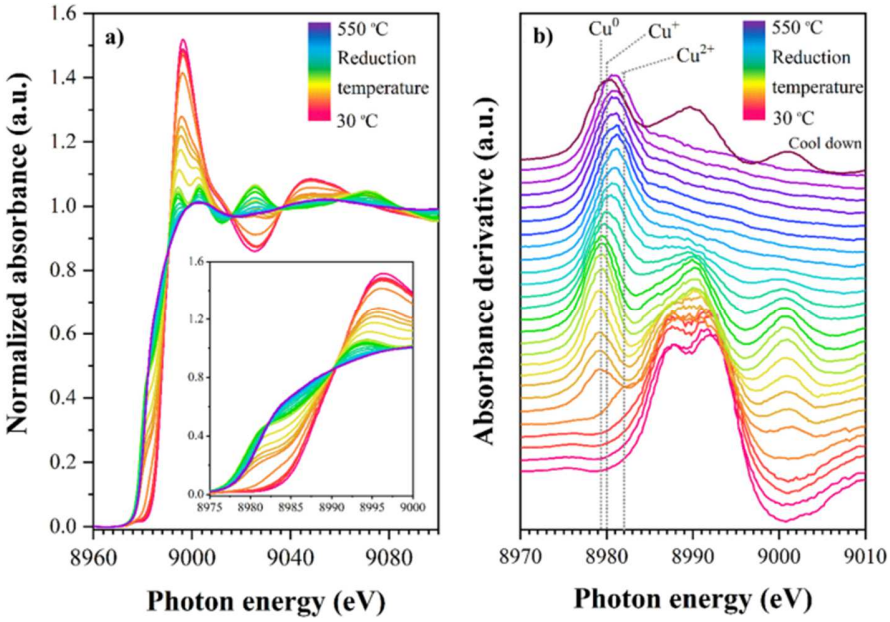

Fig. 4. *In situ* XANES spectra at Cu K-edge under H_2 TPR of the silica-supported copper phosphide with the inset showing a close-up view of the XANES region reveals a feature of pre-edge (a) and the 1st derivatization of absorbance in the pre-edge and edge (b).

These results suggested that the phase transformation was promoted by hydration and reduction processes. The paradigm shift of the electronic structure was undetected by *in situ* XRD method. Above 250 ºC, the XAS characteristic spectrum of the bivalent species almost disappeared while the features of the mono and zerovalence (Cu^0) as new species became predominant. This indicated that the formation of $Cu(PO_3)_2$ and Cu metal were in agreement with the *in situ* XRD interpretation. Above 320 ºC, the spectrum feature of Cu^+ species was predominantly observed as shown in **Fig. 4(b)**. The FT-EXAFS spectra also indicated that the Cu atoms were thoroughly coordinated by P atoms. In comparison, the Cu-Cu radial distance of 2.18 Å from the obtained Cu_3P phases by FT-EXAFS was larger than 2.05 Å reported in the reference,[48] probably due to different space groups. Interestingly, after cooling down, the Cu K-edge is the characteristic of the monovalence while the spectrum feature and FT EXAFS spectrum are different than others during the TPR process as a result of the relaxation of the crystal structures, confirmed by the XRD results.

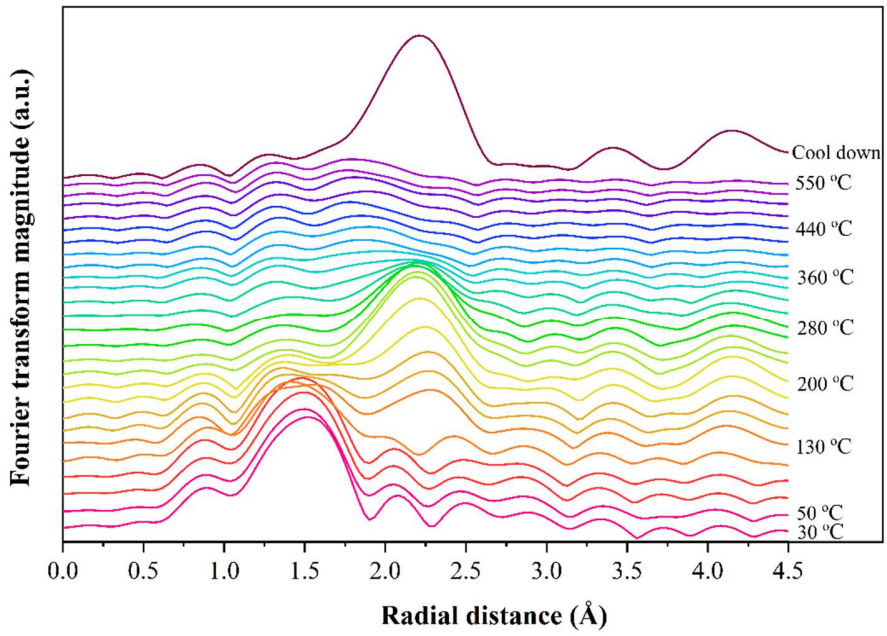

Fig. 5. Fourier transforms k^2-weighted EXAFS spectra in R space for silica-supported copper phosphide during the H_2 TPR.

According to both *in situ* characterization results, the Cu_3P/SiO_2 catalyst was successfully synthesized. The mechanism of phase transformation of the copper precursor into copper phosphide within the *in situ* H_2 reduction is proposed in **Fig. 6**. The Cu_3P phase with the $P6_3cm$ space group could serve as active sites to facilitate the conversion of guaiacol towards promising bio-oil products.

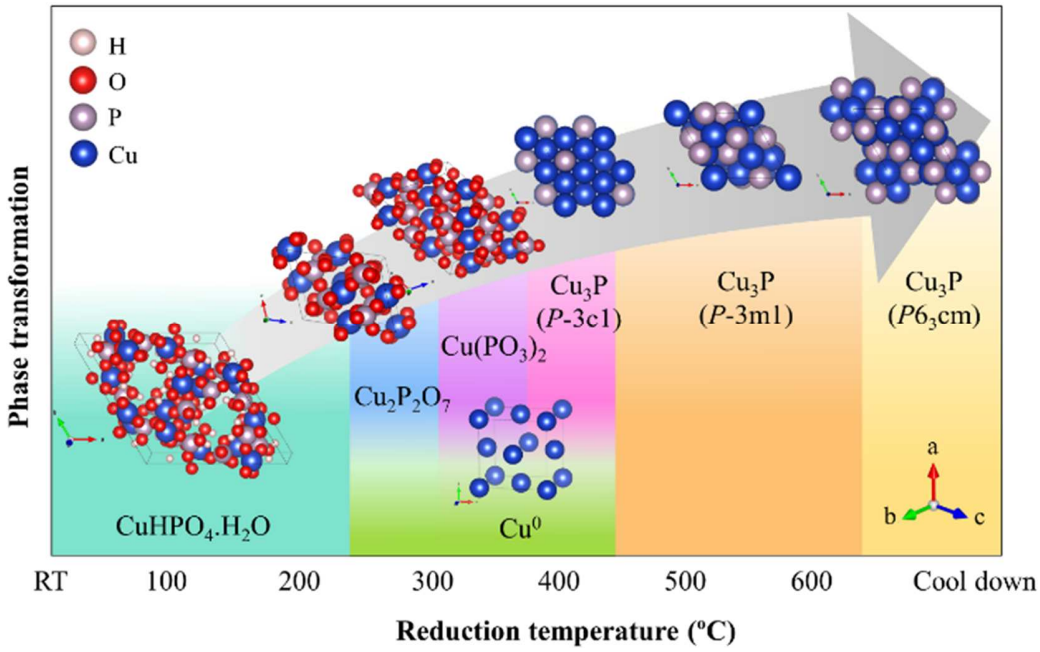

Fig. 6. Proposed mechanism of phase transformation of copper precursor to Cu_3P during *in situ* H_2 reduction (RT = room temperature).

3.4 Catalytic activity of guaiacol HDO reaction over Cu_3P catalyst

The HDO reaction of guaiacol was investigated as a function of reaction time over the Cu_3P/SiO_2 catalyst at 300 ºC in the presence of H_2. It is noted that the catalytic activity at 0 min was evaluated when the reaction temperature reached 300 ºC. The major product compound groups in the reaction mixture are classified as cyclic hydrocarbons, demethylated, deoxygenated, and methylated compounds (see detailed product distribution in Table S2 in SI). It was observed a low conversion of guaiacol (0.5%), and the main products were catechol and 2,4,6-trimethylphenol coming respectively from demethylation of guaiacol and methylation of phenol. A similar result was also reported by Ceylan and Bredenberg.[55]

From the results shown in **Fig. 7** and **Table S2** at 150 min, the highest selectivity of guaiacol HDO over Cu_3P/SiO_2 was catechol, which gradually increased while methylated compounds including xylenol and 2,4,6-trimethylphenol decreased possibly due to the deactivation of active sites by coking formation. After prolonging the reaction time to 180 min, the higher selectivity of deoxygenated compounds particularly phenol was obtained. This phenomenon was explained in detail by Lan et al.[56], showing that the properties of active species (*e.g.,* metal and P sites) on catalyst surface could alter and affected Brønsted acid sites (*i.e.,* P-OH) which are considered to be a major reason of product distribution changes. Our results show that phenol is more favorable produced via demethylation in $C_{aryl}O\text{-}CH_3$ bond of guaiacol giving catechol and CH_3^+ or CH_4 as sub-products and subsequently deoxygenation of catechol to give phenol rather than direct demethoxylation of guaiacol to phenol and methanol. A similar pathway was also reported by previous publications.[57, 58]

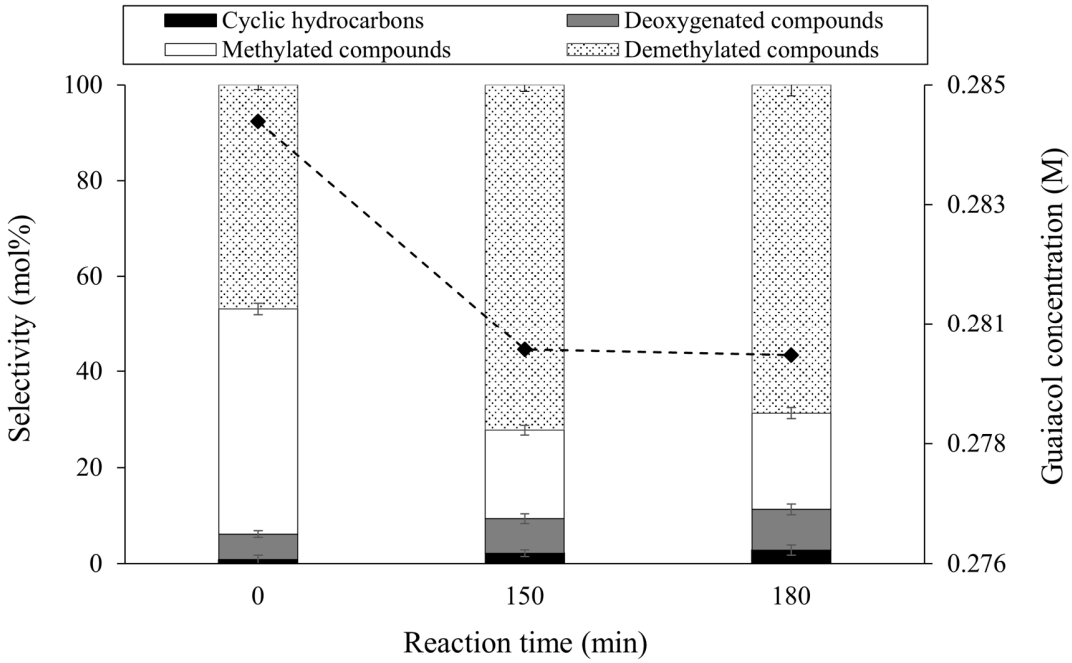

Fig. 7. Effect of reaction time on product selectivity and guaiacol concentration in the guaiacol HDO catalyzed by Cu_3P/SiO_2 at reaction condition of 300 ºC and 50 bar H_2.

Moreover, the methylated compounds consisting of xylenol, 2,4,6-trimethylphenol, and cresol were also observed, possibly as a result of acidic support-catalyzed methylation or trans-alkylation from which CH_3^+ or CH_4 was generated as sub-products during catechol production to minimize the carbon loss.[59-61] In addition, we observed slightly cyclic hydrocarbons such as cyclohexane, cyclohexene, methylcyclohexane, and 1,3-dimethyl cyclohexane after 150 min of reaction through hydrogenation of phenol. It was followed by hydrogenolysis of C_{aryl}–O bond of the intermediate product including cyclohexanol and a fully deoxygenated compound was produced. Similar pathways on non-noble metal catalysts to produce a hydrogenated product like cyclohexane were also found by Lui and co-workers.[20] There was no observation of benzene via hydrogenolysis of phenol. This result could be explained by interactions between guaiacol molecules and Cu_3P species on the catalyst surfaces.

From the above experimental results, a possible pathway of guaiacol HDO summarizing various intermediates and products as well as many elementary reactions over silica-supported copper phosphide catalyst is presented in **Fig. S2**. This corresponds to the pathway proposed by Tran and co-workers[62] and Mukundan and co-workers.[57] They proposed that demethylation and methylation of guaiacol principally took place at the onset of the reaction followed by hydrogenation and hydrogenolysis of the intermediate products. Nevertheless, the condensation and heavier products [63] such as hexamethylbenzene and biphenyl were not detected. Therefore, the used catalyst after the HDO process was further investigated by XANES. The results of the Cu K-edge XANES and Fourier transformed EXAFS spectrum in **Fig. 8** (before and after using in the reaction) show similar Cu K-edge and profile features. Accordingly, the result of Cu K-edge EXAFS fitting of the fresh sample listed in **Table S1** should be similar to the used one, implying that the local atomic structure of copper species might not change. This result could suggest that the Cu_3P/SiO_2 catalyst was stable under the HDO reaction of guaiacol.

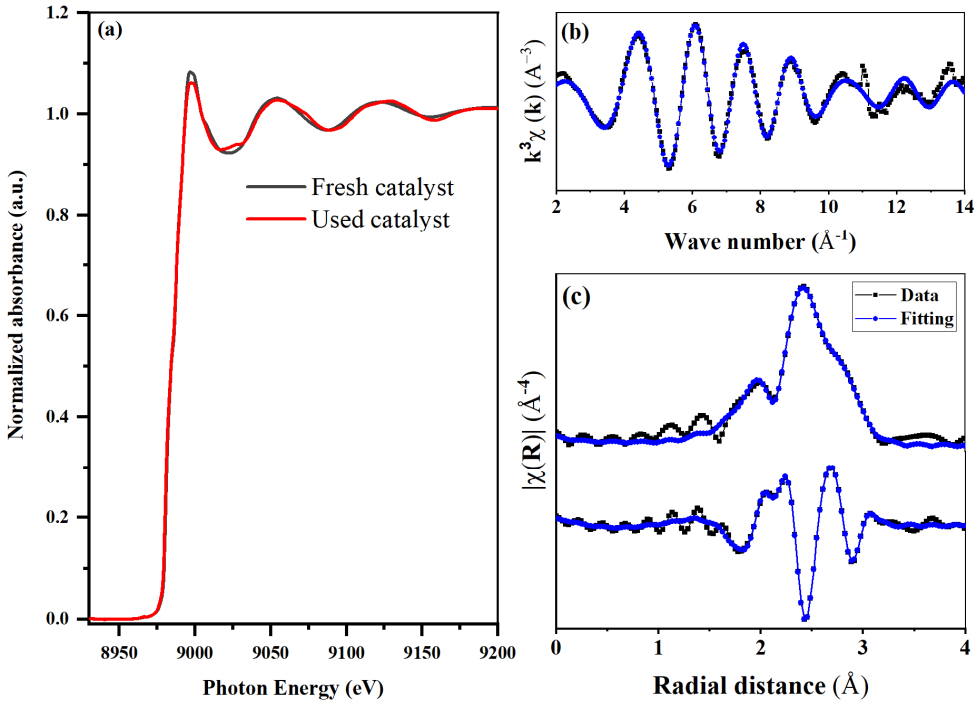

Fig. 8. (a) XANES spectra at Cu K-edge of the fresh sample (grey line) compared to the used one (red line) after the guaiacol HDO testing. Fourier transformed (FT) Cu K-edge EXAFS spectrum in (b) k space and (c) R space of the fresh Cu_3P/SiO_2 catalyst.

3.5 Active sites on the Cu_3P surfaces

According to the *in situ* XRD, *in situ* XAS and ex situ EXAFS results, the (100) and (113) facets of Cu_3P were selected to clarify the mechanism during the adsorption process on the active site because they belong to predominant peaks. The DFT calculations were performed to understand the nature of active sites on the Cu_3P surfaces. Also, the interaction between molecules/species on the Cu_3P surfaces was elucidated via the adsorption calculations. Three surface models (100), (113)A, and (113B) are illustrated in **Fig. S3** in SI. As demonstrated in **Fig. S3(c)-(e)** in SI, there are many possible active sites presented on those surfaces such as atop Cu site, atop P site, Cu-Cu bridge site, Cu-P bridge site, Cu-Cu-Cu hollow site, and Cu-P-Cu

hollow site. Many possible adsorption configurations were tested for each adsorbate. The stable configurations of the tested adsorbates (*i.e.,* guaiacol, H_2, H atom, CH_3 radical) and their E_{ads} values are demonstrated in **Fig. 9** and **Table 1**, respectively.

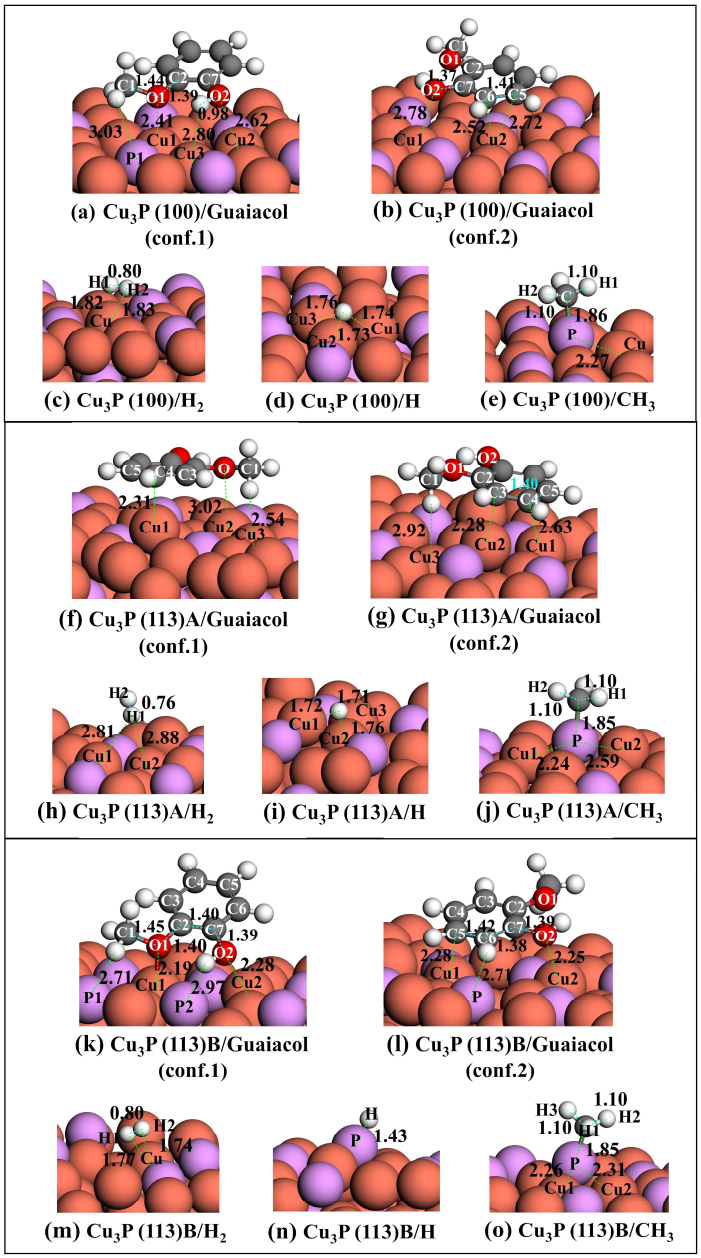

Fig. 9. Adsorption on Cu_3P surfaces (a)-(e) the (100) surface, (f)-(j) the (113)A surface and (k)-(o) the (113)B surface.

Table 1

The adsorption energies of species on the Cu_3P surfaces (in eV).

Surface	E_{ad} (eV)			
	Guaiacol	H_2	H atom	CH_3
(100)	-1.04 (conf.1)	-0.14	-2.58	-1.64
	-1.20 (conf.2)			
(113)A	-1.24 (conf.1)	-0.12	-2.88	-2.68
	-1.37 (conf.2)			
(113)B	-1.31 (conf.1)	-0.37	-3.24	-2.94
	-1.43 (conf.2)			

The adsorption calculations of guaiacol, H_2, H atom, and CH_3 on three surfaces were tested by varying possible adsorption sites. The adsorption energies of stable configurations are summarized in **Table 1**. For each adsorbate, the adsorption on the (113)B surface is more stable (or lower E_{ad}) than that on the (100) and (113)A surfaces. According to the calculated E_{ad} values, guaiacol is adsorbed much stronger than H_2. The chemisorption was observed in all guaiacol adsorption cases. It is noted that guaiacol adsorption is more energetically stable via Cu--C and Cu--OH binding modes than Cu–OCH_3 binding mode. This relates to the steric hindrance of -OCH_3 group of guaiacol. In the H_2 adsorption, the (113)B surface adsorbs H_2 stronger than the (113)A and (100) surfaces. As proposed in the literature, the local environment of the surface catalyst showed a significant role of the aromatic C_{aryl}–O bond cleavage of guaiacol, which was an important step of the HDO reaction.[64] The dehydrogenation of the methoxy group or hydroxyl group was proposed as an initial step after guaiacol adsorption leading to further

catechol or phenol formation.[64, 65] As demonstrated in **Fig. 9(k)** and **9(l)**, guaiacol is bound with the (113) surface via two O of its functional groups. Those binding modes would promote the dehydrogenation, which was the crucial step for further guaiacol conversion. In the case of a hydrogen molecule, H_2 forms chemical bonding with Cu indicating the Cu--H and H--H bond distances, but the E_{ad} of -0.36 eV indicates the low energetic stability. In the case of the H_2 on (113)A surface, both H atoms also form chemical bonds with Cu (see **Fig. 9(f)-(j)**), however, that configuration showed low energetic stability due to the E_{ad} of -0.12 eV. The physisorption of H_2 was observed on the (100) surface. In literature, the E_{ad} values of H_2, calculated from PBE-D2, are -0.08, -0.91, and -0.79 eV on the (111), (100), and (110) surfaces of the pure Cu, respectively.[66] Hydrogen adsorption on the metallic Cu is more energetically stable than the Cu_3P surfaces in this work. For all surfaces, the Cu sites are active sites for interacting with the reactant molecules (*i.e.,* guaiacol and H_2). For the (100) and (113)A surface, H prefers the hollow Cu site while CH_3 prefers the top P site as shown in **Fig. 9(a)-(j)**. In the (113)B surface, the P sites are preferred for the dissociated H atom and CH_3 radical as shown in **Fig. 9(k)-(o)**. It is noted that the (113)B surface is distorted when it adsorbs H and CH_3.

Fig. 10 reveals the Bader charge change of each adsorption configuration on the (113)B surface. As a result, the Cu sites are positively charged while the P sites are negatively charged. According to their electron-deficient aspect, the Cu sites on the Cu_3P surfaces act as the Lewis acid sites, which are in good agreement with metallic sites in other metallic phosphide catalysts (*i.e.,* RuMoP, NiMoP, FeMoP)[67]. For the guaiacol adsorption, the O atoms of the molecule show a negative partial charge approximately -1.1$|e^-|$ to -1.2$|e^-|$. When the O1 atom binds with the Cu1 sites (see **Fig. 10(a)**), its charge becomes more negative compared to another configuration in **Fig. 10(b)**. In **Fig. 10(a)**, the partial charges of bound Cu1 (+0.39$|e^-|$) and Cu2

(+0.35|e$^-$|) become more positive than those values of the pre-adsorbed surface, which are -0.28|e$^-$| deactivation of active sites by coking formation and-0.24|e$^-$|, respectively. In **Fig. 10(b)**, C5 gains more electrons when it attaches to Cu. H_2 gains electron from Cu1, where H1 is negatively charged but another H is positively charged. The H atom and •CH_3 gain electrons from the (113)B surface approximately -0.35|e$^-$| and -0.29|e$^-$|, respectively. It is noted that the H atoms at the hollow Cu site on the (100) and (113)A surfaces are less negative partial charge than those on the (113)B. In summary, the Cu sites are the active sites for adsorbing the reactants, guaiacol, and H_2, due to their local charge property. In the reactive (113)B surface, the P sites are stabilized the dissociated H and CH_3 radicals.

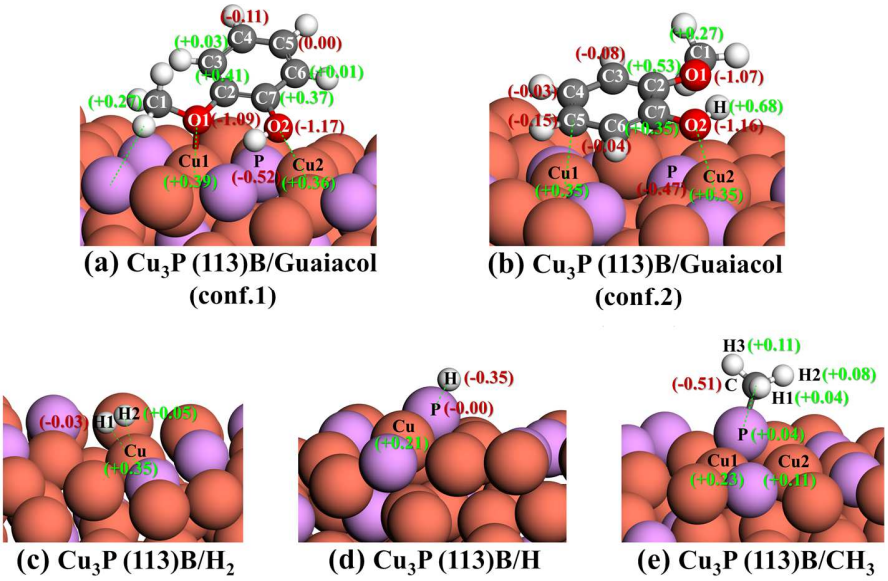

Fig. 10. Bader charge values in |e$^-$| of species adsorbed Cu_3P(113)B. The green and red values represent positive partial charge (decrease of valence electrons) and negative partial charge (increase of valence electrons), respectively.

In addition, the surface energies (γ) of the Cu_3P (100) and Cu_3P(113) were calculated. Less surface energy indicates greater stability of a surface. The details of the surface energy calculation are given in SI. As a result, the surface energies of the simulated Cu_3P(100) and Cu_3P(113) surfaces are 0.09 eV·Å^{-2} (or 1.42 J·m^{-2}) and 0.10 eV·Å^{-2} (or 1.60 J·m^{-2}), respectively. In literature, the calculated surface energies of the (111), (100), and (110) surfaces of pure Cu are 1.17, 1.28, and 1.40 J·m^{-2}, respectively.[68] The reported experimental value of Cu, the average value of all surfaces, is 1.77 J·m^{-2} [69]. Hence, the less stable Cu_3P(113) surface correlates with the better adsorption ability compared to the Cu_3P(100) surface, discussed in the previous part.

4. Conclusions

Combining *in situ* XAS and *in situ* XRD allowed us to monitor the phase transformation from $CuHPO_4.H_2O$ precursor to Cu_3P. The results from *in situ* XRD and *in situ* XANES characterizations indicated that the Cu_3P was predominated with (100) facet with +1 oxidation copper species. The combined results from DFT calculation and experimental approach reveal that the adsorption of guaiacol on the (113) surface of Cu_3P is more preferable than the (100) surface. The Cu sites on the Cu_3P surface played a predominant role in the guaiacol and H_2 adsorption. To the best of our knowledge, this is the first study that provides combined experimental catalytic testing and the computational method to study the detailed adsorption of guaiacol on Cu_3P surface. This should be beneficial for the improvement of the lignin-derived bio-oil into biofuels in the future.

Acknowledgment

The authors are grateful for the financial support from The Franco-Thai Junior Research Fellowship Program 2014 from France Embassy in Thailand and National Nanotechnology Center (P1450869, P1751332, and P1751863). This work is also supported by National Science and Technology Development Agency (NSTDA) via CAS-NSTDA Project (P1952712). Research grant for A. Junkaew is supported by the National Research Council of Thailand (NRCT5-RSA63026-02) and National Nanotechnology Center (P2051920). We also acknowledge European Synchrotron Radiation Facility (ESRF), France, and Synchrotron Light Research Institute (Public Organization: SLRI), Thailand (SUT-NANOTEC-SLRI Beamline 5.2) for the XAS facilities. We also acknowledge NSTDA Supercomputer Center (ThaiSC), Nanoscale Simulation Laboratory at National Nanotechnology Center (NANOTEC) for computation resources, and Prof. Dr. S. Seraphin (NSTDA Professional Authorship Center) for invaluable comments on manuscript preparation.

References

[1] B.M. Weckhuysen, Preface: recent advances in the in-situ characterization of heterogeneous catalysts, Chem. Soc. Rev., 39 (2010) 4557-4559. https://doi.org/10.1039/C0CS90031A.

[2] B.W.J. Chen, L. Xu, M. Mavrikakis, Computational Methods in Heterogeneous Catalysis, Chem. Rev., 121 (2021) 1007-1048. https://doi.org/10.1021/acs.chemrev.0c01060.

[3] B.M. Weckhuysen, In-situ spectroscopy of catalysts, in: In-situ spectroscopy of catalysts, American Scientific Publishers, 2004, pp. 1-11.

[4] C. Tsakonas, M. Dimitropoulos, A.C. Manikas, C. Galiotis, Growth and in situ characterization of 2D materials by chemical vapour deposition on liquid metal catalysts: a review, Nanoscale, 13 (2021) 3346-3373. https://doi.org/10.1039/D0NR07330J.

[5] C.-J. Chang, Y. Zhu, J. Wang, H.-C. Chen, C.-W. Tung, Y.-C. Chu, H.M. Chen, In situ X-ray diffraction and X-ray absorption spectroscopy of electrocatalysts for energy conversion reactions, J. Mater. Chem. A, 8 (2020) 19079-19112. https://doi.org/10.1039/D0TA06656G.

[6] T. Daley, K.B. Opuni, E. Raj, A.J. Dent, G. Cibin, T.I. Hyde, G. Sankar, Monitoring the process of formation of ZnO from ZnO_2 using in situ combined XRD/XAS technique, J. Phys. Conden. Matter, 33 (2021) 264002. https://doi.org/10.1088/1361-648x/abfb91.

[7] N. Kochaputi, P. Khemthong, P. Kasamechonchung, T. Butburee, W. Limphirat, Y. Poo-arporn, S. Kuboon, K. Faungnawakij, C. Kongmark, Roles of supports on reducibility and activities of Cu_3P catalysts for deoxygenation of oleic acid: In situ XRD and XAS studies, Molec. Catal., (2021) 111425. https://doi.org/10.1016/j.mcat.2021.111425.

[8] Y. Zhu, T.-R. Kuo, Y.-H. Li, M.-Y. Qi, G. Chen, J. Wang, Y.-J. Xu, H.M. Chen, Emerging dynamic structure of electrocatalysts unveiled by in situ X-ray diffraction/absorption spectroscopy, Energy Environ. Sci., 14 (2021) 1928-1958. https://doi.org/10.1039/D0EE03903A.

[9] N. Azevedo, J.A. Neto, P. de Matos, A. Betioli, M. Szeląg, P. Gleize, Utilization of Thermally Treated SiC Nanowhiskers and Superplasticizer for Cementitious Composite Production, Materials, 14 (2021) 4062. https://doi.org/

[10] Y. Gambo, S. Adamu, A.A. Abdulrasheed, R.A. Lucky, M.S. Ba-Shammakh, M.M. Hossain, Catalyst design and tuning for oxidative dehydrogenation of propane – A

review, Appl. Catal. A, Gen., 609 (2021) 117914. https://doi.org/https://doi.org/10.1016/j.apcata.2020.117914.

[11] Y. Wongnongwa, S. Jungsuttiwong, M. Pimsuta, P. Khemthong, M. Kunaseth, Mechanistic and thermodynamic insights into the deoxygenation of palm oils using Ni_2P catalyst: A combined experimental and theoretical study, Chem. Eng. J., 399 (2020) 125586. https://doi.org/10.1016/j.cej.2020.125586.

[12] I.B. Adilina, N. Rinaldi, S.P. Simanungkalit, F. Aulia, F. Oemry, G.B.G. Stenning, I.P. Silverwood, S.F. Parker, Hydrodeoxygenation of guaiacol as a bio-oil model compound over pillared clay-supported nickel–molybdenum catalysts, J. Phys. Chem. C, 123 (2019) 21429-21439. https://doi.org/10.1021/acs.jpcc.9b01890.

[13] E.A. Roldugina, E.R. Naranov, A.L. Maximov, E.A. Karakhanov, Hydrodeoxygenation of guaiacol as a model compound of bio-oil in methanol over mesoporous noble metal catalysts, Appl. Catal. A, Gen., 553 (2018) 24-35. https://doi.org/10.1016/j.apcata.2018.01.008.

[14] I.D. Mora-Vergara, L. Hernández Moscoso, E.M. Gaigneaux, S.A. Giraldo, V.G. Baldovino-Medrano, Hydrodeoxygenation of guaiacol using NiMo and CoMo catalysts supported on alumina modified with potassium, Catal. Today, 302 (2018) 125-135. https://doi.org/10.1016/j.cattod.2017.07.015.

[15] S. Rakmae, N. Osakoo, M. Pimsuta, K. Deekamwong, C. Keawkumay, T. Butburee, K. Faungnawakij, C. Geantet, S. Prayoonpokarach, J. Wittayakun, P. Khemthong, Defining nickel phosphides supported on sodium mordenite for hydrodeoxygenation of palm oil, Fuel Process. Technol., 198 (2020) 106236. https://doi.org/10.1016/j.fuproc.2019.106236.

[16] T. Guo, Q. Xia, Y. Shao, X. Liu, Y. Wang, Direct deoxygenation of lignin model compounds into aromatic hydrocarbons through hydrogen transfer reaction, Appl. Catal. A, Gen., 547 (2017) 30-36. https://doi.org/10.1016/j.apcata.2017.07.050.

[17] X. Besse, Y. Schuurman, N. Guilhaume, Reactivity of lignin model compounds through hydrogen transfer catalysis in ethanol/water mixtures, Appl. Catal. B, Environ., 209 (2017) 265-272. https://doi.org/10.1016/j.apcatb.2017.03.013.

[18] M. Hellinger, H.W. Carvalho, S. Baier, D. Wang, W. Kleist, J.-D.J.A.C.A.G. Grunwaldt, Catalytic hydrodeoxygenation of guaiacol over platinum supported on metal oxides and zeolites, Appl. Catal. A, Gen., 490 (2015) 181-192. https://doi.org/10.1016/j.apcata.2014.10.043.

[19] R.H. Venderbosch, A.R. Ardiyanti, J. Wildschut, A. Oasmaa, H.J. Heeres, Stabilization of biomass-derived pyrolysis oils, J. Chem. Technol. Biotechnol., 85 (2010) 674-686. https://doi.org/10.1002/jctb.2354.

[20] X. Wang, S. Zhu, S. Wang, Y. He, Y. Liu, J. Wang, W. Fan, Y. Lv, Low temperature hydrodeoxygenation of guaiacol into cyclohexane over Ni/SiO_2 catalyst combined with Hβ zeolite, RSC Adv., 9 (2019) 3868-3876. https://doi.org/10.1039/C8RA09972C.

[21] R. Shu, R. Li, B. Lin, B. Luo, Z. Tian, High dispersed Ru/SiO_2-ZrO_2 catalyst prepared by polyol reduction method and its catalytic applications in the hydrodeoxygenation of phenolic compounds and pyrolysis lignin-oil, Fuel, 265 (2020) 116962. https://doi.org/10.1016/j.fuel.2019.116962.

[22] X. Liu, W. Jia, G. Xu, Y. Zhang, Y. Fu, Selective hydrodeoxygenation of lignin-derived phenols to cyclohexanols over Co-based catalysts, ACS Sustain. Chem. Eng., 5 (2017) 8594-8601. https://doi.org/10.1021/acssuschemeng.7b01047.

[23] D.J. Rensel, S. Rouvimov, M.E. Gin, J.C. Hicks, Highly selective bimetallic FeMoP catalyst for C–O bond cleavage of aryl ethers, J. Catal., 305 (2013) 256-263. https://doi.org/10.1016/j.jcat.2013.05.026.

[24] M. Alda-Onggar, P. Mäki-Arvela, A. Aho, I.L. Simakova, D.Y. Murzin, Hydrodeoxygenation of phenolic model compounds over zirconia supported Ir and Ni-catalysts, React. Kinet. Mech. Catal., 126 (2019) 737-759. https://doi.org/10.1007/s11144-018-1502-1.

[25] Z. He, X.J.F.o.C.S. Wang, Engineering, Highly selective catalytic hydrodeoxygenation of guaiacol to cyclohexane over Pt/TiO_2 and $NiMo/Al_2O_3$ catalysts, Front. Chem. Sci. Eng., 8 (2014) 369-377. https://doi.org/10.1007/s11705-014-1435-9.

[26] D.-Y. Hong, S.J. Miller, P.K. Agrawal, C.W. Jones, Hydrodeoxygenation and coupling of aqueous phenolics over bifunctional zeolite-supported metal catalysts, Chem. Commun., 46 (2010) 1038-1040. https://doi.org/10.1039/B918209H.

[27] X. Zhou, X.-Y. Wei, Z.-Q. Liu, J.-H. Lv, Y.-L. Wang, Z.-K. Li, Z.-M. Zong, Highly selective catalytic hydroconversion of benzyloxybenzene to bicyclic cyclanes over bifunctional nickel catalysts, Catal. Commun., 98 (2017) 38-42. https://doi.org/10.1016/j.catcom.2017.04.042.

[28] G. Yao, G. Wu, W. Dai, N. Guan, L. Li, Hydrodeoxygenation of lignin-derived phenolic compounds over bi-functional Ru/H-Beta under mild conditions, Fuel, 150 (2015) 175-183. https://doi.org/10.1016/j.fuel.2015.02.035.

[29] R. Paul, S.C. Shit, T. Fovanna, D. Ferri, B. Srinivasa Rao, G.K.K. Gunasooriya, D.Q. Dao, Q.V. Le, I. Shown, M.P.J.A.A.M. Sherburne, Interfaces, Realizing catalytic acetophenone hydrodeoxygenation with palladium-equipped porous organic polymers,

ACS Appl. Mater. Interfaces, 12 (2020) 50550-50565. https://doi.org/10.1021/acsami.0c16680.

[30] C. Sarkar, S.C. Shit, D.Q. Dao, J. Lee, N.H. Tran, R. Singuru, K. An, D.N. Nguyen, Q. Van Le, P.N.J.G.C. Amaniampong, An efficient hydrogenation catalytic model hosted in a stable hyper-crosslinked porous-organic-polymer: From fatty acid to bio-based alkane diesel synthesis, Green Chem., 22 (2020) 2049-2068. https://doi.org/10.1039/C9GC03803E.

[31] R. Prins, M.E. Bussell, Metal phosphides: preparation, characterization and catalytic reactivity, Catal. Lett., 142 (2012) 1413-1436. https://doi.org/10.1007/s10562-012-0929-7.

[32] J.-S. Moon, E.-G. Kim, Y.-K. Lee, Active sites of Ni_2P/SiO_2 catalyst for hydrodeoxygenation of guaiacol: a joint XAFS and DFT study, J. Catal., 311 (2014) 144-152. https://doi.org/10.1016/j.jcat.2013.11.023.

[33] J.A. Cecilia, A. Infantes-Molina, E. Rodríguez-Castellón, A. Jiménez-López, S.T. Oyama, Oxygen-removal of dibenzofuran as a model compound in biomass derived bio-oil on nickel phosphide catalysts: role of phosphorus, Appl. Catal. B, Environ., 136-137 (2013) 140-149. https://doi.org/10.1016/j.apcatb.2013.01.047.

[34] P. Bui, J.A. Cecilia, S.T. Oyama, A. Takagaki, A. Infantes-Molina, H. Zhao, D. Li, E. Rodríguez-Castellón, A.J.J.J.o.C. López, Studies of the synthesis of transition metal phosphides and their activity in the hydrodeoxygenation of a biofuel model compound, J. Catal., 294 (2012) 184-198. https://doi.org/

[35] M. Ruangudomsakul, N. Osakoo, J. Wittayakun, C. Keawkumay, T. Butburee, S. Youngjan, K. Faungnawakij, Y. Poo-arporn, P. Kidkhunthod, P. Khemthong,

Hydrodeoxygenation of palm oil to green diesel products on mixed-phase nickel phosphides, Molec. Catal., (2021) 111422. https://doi.org/https://doi.org/10.1016/j.mcat.2021.111422.

[36] J. Zhang, K. Matsubara, G.-N. Yun, H. Zheng, A. Takagaki, R. Kikuchi, S.T.J.A.C.A.G. Oyama, Comparison of phosphide catalysts prepared by temperature-programmed reduction and liquid-phase methods in the hydrodeoxygenation of 2-methylfuran, Appl. Catal. A, Gen., 548 (2017) 39-46. https://doi.org/

[37] J. Zakzeski, P.C.A. Bruijnincx, A.L. Jongerius, B.M. Weckhuysen, The catalytic valorization of lignin for the production of renewable chemicals, Chem. Rev., 110 (2010) 3552-3599. https://doi.org/10.1021/cr900354u.

[38] M.P. Pandey, C.S. Kim, Lignin depolymerization and conversion: a review of thermochemical methods, Chem. Eng. Technol., 34 (2011) 29-41. https://doi.org/10.1002/ceat.201000270.

[39] S. Pithakratanayothin, R. Tongsri, T. Chaisuwan, S. Wongkasemjit, P. Khemthong, S. Limpijumnong, P. Pharanchai, K. Malaicharoen, Discovery of mono(u-oxo)dicopper and bis(u-oxo)dicopper in ordered Cu incorporated in SBA-15 via sol-gel process from silatrane at room temperature: An in situ XAS investigation, Micropor. Mesopor. Mater., 301 (2020) 110225. https://doi.org/10.1016/j.micromeso.2020.110225.

[40] P. Khemthong, C. Kongmark, N. Kochaputi, S. Mahakot, S. Rodporn, K. Faungnawakij, In situ X-ray absorption fine structure probing-phase evolution of $CuFe_2O_4$ in nanospace confinement, Inorg. Chem., 58 (2019) 6584-6587. https://doi.org/10.1021/acs.inorgchem.9b00540.

[41] B. Ravel, M. Newville, ATHENA, ARTEMIS, HEPHAESTUS: data analysis for X-ray absorption spectroscopy using IFEFFIT, J. Synchrotron Radiat., 12 (2005) 537-541. https://doi.org/10.1107/S0909049505012719.

[42] G. Kresse, J. Furthmüller, Efficient iterative schemes for ab initio total-energy calculations using a plane-wave basis set, Phys. Rev. B, 54 (1996) 11169-11186. https://doi.org/10.1103/PhysRevB.54.11169.

[43] G. Kresse, Ab initio molecular dynamics for liquid metals, J. Non-Crystal. Solids, 192-193 (1995) 222-229. https://doi.org/10.1016/0022-3093(95)00355-X.

[44] G. Kresse, D. Joubert, From ultrasoft pseudopotentials to the projector augmented-wave method, Phys. Rev. B, 59 (1999) 1758-1775. https://doi.org/10.1103/PhysRevB.59.1758.

[45] J. Paier, R. Hirschl, M. Marsman, G. Kresse, The Perdew–Burke–Ernzerhof exchange-correlation functional applied to the G2-1 test set using a plane-wave basis set, J. Chem. Phys., 122 (2005) 234102. https://doi.org/10.1063/1.1926272.

[46] S. Grimme, J. Antony, S. Ehrlich, H. Krieg, A consistent and accurate ab initio parametrization of density functional dispersion correction (DFT-D) for the 94 elements H-Pu, J. Chem. Phys., 132 (2010) 154104. https://doi.org/10.1063/1.3382344.

[47] M.C. Alvarez-Galvan, G. Blanco-Brieva, M. Capel-Sanchez, S. Morales-delaRosa, J.M. Campos-Martin, J.L.G. Fierro, Metal phosphide catalysts for the hydrotreatment of non-edible vegetable oils, Catal. Today, 302 (2018) 242-249. https://doi.org/10.1016/j.cattod.2017.03.031.

[48] G. Yuan, J. Bai, B. Gao, L. Ren, J. Mei, L. Zhang, The effect of crystal facet (312) exposure intensity of $Ni_{12}P_5$ nanoparticle on its hydrodechlorination catalytic activity,

Inorg. Chem. Commun., 111 (2020) 107595. https://doi.org/10.1016/j.inoche.2019.107595.

[49] N. Kochaputi, C. Kongmark, P. Khemthong, T. Butburee, S. Kuboon, A. Worayingyong, K. Faungnawakij, Catalytic behaviors of supported Cu, Ni, and Co phosphide catalysts for deoxygenation of oleic acid, Catalysts, 9 (2019) 715. https://doi.org/10.3390/catal9090715.

[50] C. Stinner, Z. Tang, M. Haouas, T. Weber, R. Prins, Preparation and ^{31}P NMR characterization of nickel phosphides on silica, J. Catal., 208 (2002) 456-466. https://doi.org/10.1006/jcat.2002.3577.

[51] H. Pfeiffer, F. Tancret, T. Brousse, Synthesis, characterization and electrochemical properties of copper phosphide (Cu_3P) thick films prepared by solid-state reaction at low temperature: a probable anode for lithium ion batteries, Electrochim. Acta, 50 (2005) 4763-4770. https://doi.org/10.1016/j.electacta.2005.02.024.

[52] L. Li, C. Han, L. Yang, X. Wang, B. Zhang, The Nature of PH_3 decomposition reaction over amorphous CoNiBP alloy supported on carbon nanotubes, Ind. Eng. Chem. Res., 49 (2010) 1658-1662. https://doi.org/10.1021/ie9015478.

[53] Y. Li, M. Kong, J. Hu, J. Zhou, Carbon-microcuboid-supported phosphorus-coordinated single atomic copper with ultrahigh content and its abnormal modification to Na storage behaviors, Adv. Energy Mater., 10 (2020) 2000400. https://doi.org/10.1002/aenm.202000400.

[54] S.L. Bergman, S. Dahlin, V.V. Mesilov, Y. Xiao, J. Englund, S. Xi, C. Tang, M. Skoglundh, L.J. Pettersson, S.L. Bernasek, In-situ studies of oxidation/reduction of

copper in Cu-CHA SCR catalysts: comparison of fresh and SO_2-poisoned catalysts, Appl. Catal. B, Environ., 269 (2020) https://doi.org/10.1016/j.apcatb.2020.118722.

[55] R. Ceylan, J.B.s. Bredenberg, Hydrogenolysis and hydrocracking of the carbon-oxygen bond. 2. Thermal cleavage of the carbon-oxygen bond in guaiacol, Fuel, 61 (1982) 377-382. https://doi.org/10.1016/0016-2361(82)90054-0.

[56] X. Lan, E.J. Hensen, T.J.A.C.A.G. Weber, Hydrodeoxygenation of guaiacol over Ni_2P/SiO_2–reaction mechanism and catalyst deactivation, 550 (2018) 57-66. https://doi.org/

[57] S. Mukundan, M. Konarova, L. Atanda, Q. Ma, J. Beltramini, Guaiacol hydrodeoxygenation reaction catalyzed by highly dispersed, single layered MoS_2/C, Catal. Sci. Technol., 5 (2015) 4422-4432. https://doi.org/10.1039/C5CY00607D.

[58] E. Laurent, B. Delmon, Influence of water in the deactivation of a sulfided NiMoγ-Al_2O_3 catalyst during hydrodeoxygenation, J. Catal., 146 (1994) 281-291. https://doi.org/10.1016/0021-9517(94)90032-9.

[59] G.W. Huber, A. Corma, Synergies between bio- and oil refineries for the production of fuels from biomass, Angew. Chem. Int. Ed., 46 (2007) 7184-7201. https://doi.org/10.1002/anie.200604504.

[60] X. Zhu, L.L. Lobban, R.G. Mallinson, D.E. Resasco, Bifunctional transalkylation and hydrodeoxygenation of anisole over a Pt/HBeta catalyst, J. Catal., 281 (2011) 21-29. https://doi.org/10.1016/j.jcat.2011.03.030.

[61] A. Gutierrez, R.K. Kaila, M.L. Honkela, R. Slioor, A.O.I. Krause, Hydrodeoxygenation of guaiacol on noble metal catalysts, Catal. Today, 147 (2009) 239-246. https://doi.org/10.1016/j.cattod.2008.10.037.

[62] N.T.T. Tran, Y. Uemura, S. Chowdhury, A. Ramli, Vapor-phase hydrodeoxygenation of guaiacol on Al-MCM-41 supported Ni and Co catalysts, Appl. Catal. A, Gen., 512 (2016) 93-100. https://doi.org/10.1016/j.apcata.2015.12.021.

[63] V.N. Bui, D. Laurenti, P. Afanasiev, C. Geantet, Hydrodeoxygenation of guaiacol with CoMo catalysts. Part I: Promoting effect of cobalt on HDO selectivity and activity, Appl. Catal. B, Environ., 101 (2011) 239-245. https://doi.org/10.1016/j.apcatb.2010.10.025.

[64] C.-C. Chiu, A. Genest, A. Borgna, N. Rösch, Hydrodeoxygenation of guaiacol over Ru(0001): a DFT study, ACS Catal., 4 (2014) 4178-4188. https://doi.org/10.1021/cs500911j.

[65] Q.T. Trinh, A. Banerjee, K.B. Ansari, D.Q. Dao, A. Drif, N.T. Binh, D.T. Tung, P.M.Q. Binh, P.N. Amaniampong, P.T. Huyen, Upgrading of Bio-oil from Biomass Pyrolysis: Current Status and Future Development, in: S. Nanda, D.-V.N. Vo, P.K. Sarangi (Eds.) Biorefinery of Alternative Resources: Targeting Green Fuels and Platform Chemicals, 2020, pp. 317-353.

[66] L. Álvarez-Falcón, F. Viñes, A. Notario-Estévez, F. Illas, On the hydrogen adsorption and dissociation on Cu surfaces and nanorows, Surf. Sci., 646 (2016) 221-229. https://doi.org/10.1016/j.susc.2015.08.005.

[67] V. Jain, Y. Bonita, A. Brown, A. Taconi, J.C. Hicks, N. Rai, Mechanistic insights into hydrodeoxygenation of phenol on bimetallic phosphide catalysts, Catal. Sci. Technol., 8 (2018) 4083-4096. https://doi.org/10.1039/C8CY00977E.

[68] S. Foiles, M. Baskes, M. Daw, Erratum: Embedded-atom-method functions for the fcc metals Cu, Ag, Au, Ni, Pd, Pt, and their alloys, Phys. Rev. B, 37 (1988) 10378. https://doi.org/10.1103/PhysRevB.33.7983.

[69] W. Tyson, W. Miller, Surface free energies of solid metals: Estimation from liquid surface tension measurements, Surf. Sci., 62 (1977) 267-276. https://doi.org/10.1016/0039-6028(77)90442-3.

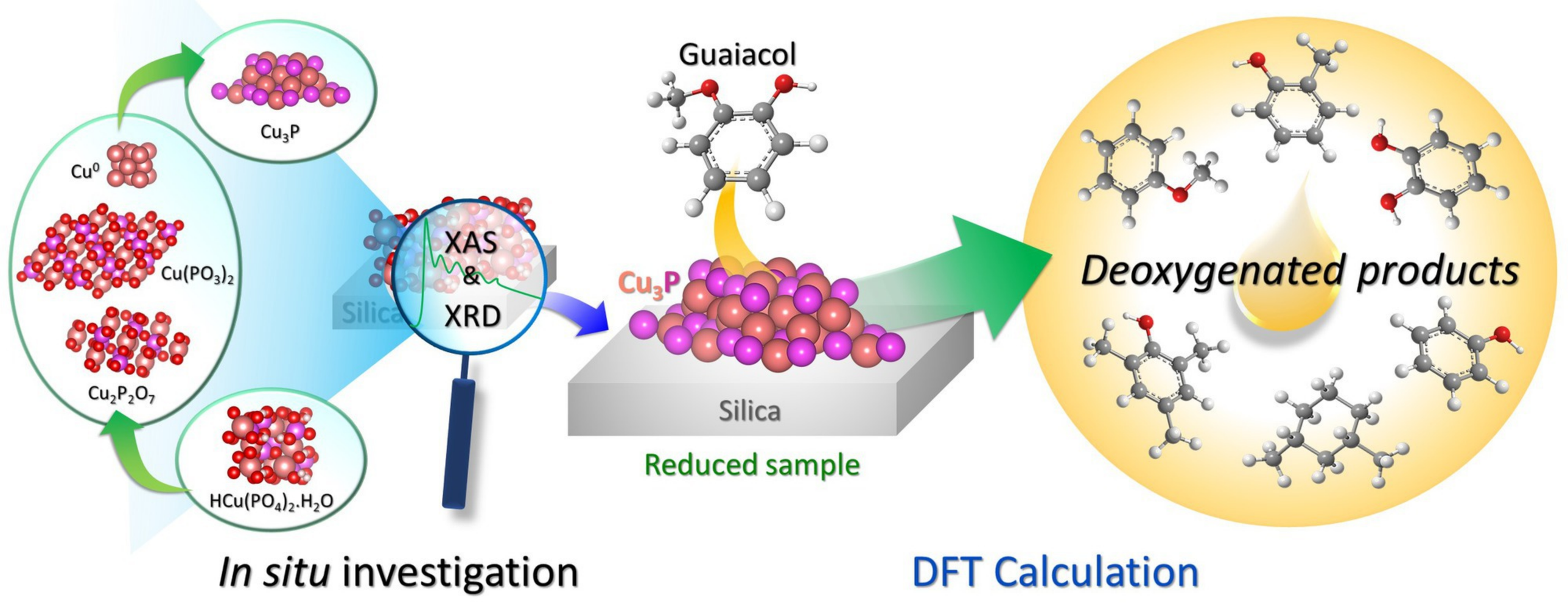
Cu3P
Cu0
Cu(PO3)2
Cu2P2O7
HCu(PO4)2.H2O
XAS
&
XRD
Silica
Guaiacol
Cu3P
Silica
Reduced sample
Deoxygenated products
In situ investigation
DFT Calculation